Desalination 602 (2025) 118638

Contents lists available at ScienceDirect

Desalination

journal homepage: www.elsevier.com/locate/desal

Activated carbons for flow electrode capacitive deionization (FCDI) – Morphological, electrochemical and rheological analysis☆

H.M. Saif [a], B. Ferrández-Gómez [b], V.D. Alves [c], R.M. Huertas [d], G. Alemany-Molina [e,f], A. Viegas [c], E. Morallón [e,g], D. Cazorla-Amorós [e,f], J.G. Crespo [a,h], S. Pawlowski [a,*]

[a] LAQV-REQUIMTE, DQ, FCT, Universidade NOVA de Lisboa, 2829-516 Caparica, Portugal
[b] Department of Biochemistry, Molecular Biology, Edaphology and Agricultural Chemistry, University of Alicante, 03690 Alicante, Spain
[c] LEAF—Linking Landscape, Environment, Agriculture and Food, Associated Laboratory TERRA, Instituto Superior de Agronomia, Universidade de Lisboa, Tapada da Ajuda, 1349-017 Lisboa, Portugal
[d] iBET – Instituto de Biologia Experimental e Tecnológica, Apartado 12, 2781-901 Oeiras, Portugal
[e] Materials Institute of Alicante, University of Alicante, 03690 Alicante, Spain
[f] Department of Inorganic Chemistry, University of Alicante, 03690 Alicante, Spain
[g] Department of Physical Chemistry, University of Alicante, 03690 Alicante, Spain
[h] Instituto de Tecnologia Química e Biológica António Xavier, Universidade NOVA de Lisboa, Av. da República, 2780-157 Oeiras, Portugal

GRAPHICAL ABSTRACT

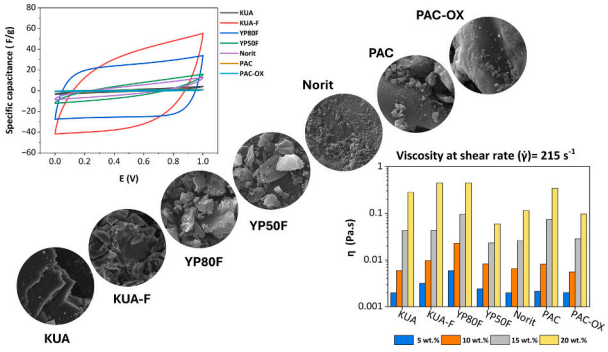

ARTICLE INFO

Keywords:
Flow electrode capacitive deionization (FCDI)
Activated carbons
Surface chemistry
Particle size reduction
Desalination
Salt adsorption capacity

ABSTRACT

Flow electrode capacitive deionization (FCDI) is a desalination technology employing flowable carbon slurries to remove salt from an influent through the electro-sorption of ions at the surface of pores of activated carbon particles. This study presents an extensive morphological, electrochemical and rheological analysis of flow electrodes prepared using commercial (YP50F, YP80F, Norit, PAC) and lab-synthesized (KUA, PAC-OX) activated carbons. Simultaneous optimization of particle size, surface area, and surface chemistry of activated carbons is essential to enhance desalination efficiency in FCDI applications. The lab-made highly microporous activated carbon (KUA), prepared from a Spanish anthracite, exhibited a remarkably high specific surface area (~2800 m^2/g) but required first a particle size reduction through ball milling (from 56 μm to 12 μm) for the respective

☆ This article is part of a special issue entitled: Desalination technology published in Desalination.

* Corresponding author.
E-mail address: s.pawlowski@fct.unl.pt (S. Pawlowski).

https://doi.org/10.1016/j.desal.2025.118638
Received 4 December 2024; Received in revised form 14 January 2025; Accepted 30 January 2025
Available online 1 February 2025

flow electrodes to achieve flowability. The slurry of milled fine KUA (designated as KUA—F) shows a specific capacitance of 55 F/g, a 38-fold increase compared to its pristine form. The KUA-F flow electrode also achieved a maximum salt adsorption capacity of 185 mg/g, outperforming the leading commercial alternative (YP80F) by 26 %. The FCDI cell with the KUA-F flow electrode exhibited a desalination efficiency of 79 % at 15 wt% loading, surpassing YP80F by 29 %. In contrast, using PAC-OX (oxidized form of PAC), despite increasing oxygen functional groups and with relatively higher specific surface area, led only to a 2 % improvement in desalination performance, highlighting that oxidation alone at larger particle sizes and broader distribution is insufficient.

1. Introduction

The global population is expanding at an unprecedented rate, and the demand for freshwater in the agricultural, industrial, and residential sectors is rising. According to the 2017 United Nations World Water Assessment Program (WWAP) report, a global water deficit of 40 % is anticipated by 2030 [1,2]. In response to this growing crisis, water desalination has become increasingly important in addressing this issue, driving the development of innovative and efficient technologies. Flow electrode capacitive deionization (FCDI) that utilizes flowable electrodes (activated carbon slurries) has gained significant limelight as a promising desalination technology, as it offers several benefits over traditional capacitive deionization (CDI) [3–5]. For example, it simplifies the scaling-up process by allowing continuous desalination without the need for *ex-situ* electrode regeneration. Additionally, flowable electrodes achieve better ion adsorption due to more exposed and easily assessable activated carbon (AC) pores [6–9]. In addition to desalination, FCDI technology has been investigated for selective recovery applications, including lithium extraction from brines, phosphorus recovery, uranium and sulfate removal from acid-contaminated groundwater, and the elimination of organic pollutants for water purification [10–15].

Ideal flow electrodes should possess a significantly high specific surface area with abundant ion adsorption sites, the ability to maintain flowability even at high mass loadings, high conductivity and ion mobility, and hydrophilicity to guarantee the effective contact between the electrode's particle porous structure and aqueous electrolyte. Additionally, they must be electrochemically stable and economically viable in terms of cost, availability, and recyclability [16]. Carbon-based materials, particularly activated carbons (AC), are widely used in FCDI due to their ability to meet these requirements [17–19].

Investigating different kinds of ACs and their modified forms has been the focus of research efforts to enhance the performance of flow electrodes. Commercially available ACs specifically developed for supercapacitor applications, such as YP50F and YP80F, have been widely studied due to their high surface areas and well-developed porosity, which are essential for enhancing ion adsorption in FCDI systems [7,15,20–23]. Incorporation of conductive additives like carbon black and carbon nanotubes (CNTs) into the AC slurry can optimize the electronic conductivity and facilitate a more efficient ion removal. Nevertheless, the hydrophobic nature of these additives leads to a considerable increase in slurry viscosity, which in turn limits the AC mass loading to lower levels [24–26]. To enhance carbon mass loading in flow electrodes, Hatzell et al. [19] successfully modified the surface of YP50F (uniform particle size ~10 μm) through oxidation, which improved the hydrophilicity and wettability of this carbon material. As a result, an 8 wt% increase in carbon mass loading was accomplished. However, the effects of oxidizing AC particles with large particle sizes and broad-size distributions on desalination performance have yet to be explored.

On the other hand, if we consider ACs, which are commonly used in water treatment applications, they lack in high specific surface areas due to their limited porosity, which restricts charge storage, while their tortuous porosity hinders ion diffusion, leading to lower adsorption capacity. To overcome these issues, new ACs with a specific surface area greater than 2000 m^2/g and a high volume of mesopores and micropores, known as super-activated carbons, are increasingly being developed [27]. In this context, Zhang et al. [28] have shown that micropores can increase the specific surface area and provide an effective electrical double layer for ion electro-sorption, while mesopores can reduce the resistance to ion diffusion. This results in a higher surface area availability for ion adsorption and, thus, a higher FCDI desalination efficiency. To achieve these morphological properties, the synthesis process of ACs must involve chemical activation with KOH, NaOH, or H_3PO_4, as it offers better properties compared to physical activation, such as higher specific surface area, greater number of functional groups, shorter preparation time, and higher product yield [29–32].

In this study, an AC material named KUA, with a very high specific surface (~2800 m^2/g), prepared from Spanish anthracite by chemical activation using KOH, was used for the first time to prepare flow electrodes. Other flow electrodes prepared when using commercially available ACs, including YP80F, YP50F, Norit, and Powdered Acticarbone® (PAC), were also tested. Their electrochemical, morphological, and rheological properties were thoroughly investigated. In addition, desalination efficiency, desalination rate, current efficiency and specific energy consumption of FCDI with different activated carbons at 5 wt%, 10 wt% and 15 wt% of mass loading in the flow electrodes were comprehensively evaluated. Furthermore, to study the impact of surface chemistry while keeping other factors constant, the oxidized version of PAC (PAC-OX) was prepared and tested as all other carbons. This AC has a larger particle size and broader size distribution, but a similar specific surface area compared to the YP50F. This approach allows to assess how carbon surface oxidation, when using carbon materials with larger particle sizes and broader size distribution, affects the desalination performance in FCDI applications.

2. Materials and methods

2.1. Materials

The following commercially available activated carbons (ACs) were used: YP80F and YP50F, specifically designed for electric double-layer capacitors, were purchased from Chemviron, Germany. Norit, a steam-activated and acid-washed carbon, was obtained from Alfa Aesar, Germany. Powdered Acticarbone® (PAC), typically used in water treatment applications, was purchased from CalgonCarbon, Germany. Nitric acid (ACS Reagent, 70 %, Honeywell Fluka™) was used to oxidize the PAC to obtain the PAC-OX. NaCl salt (Honeywell Fluka™ Chemicals, Germany) was used to prepare the electrolyte and feed solution. Milli-Q water (Millipore), with approximately 18 MΩ cm, was used to prepare all solutions.

2.2. Preparation of lab-made activated carbons

2.2.1. Synthesis of KUA activated carbon

The super porous AC (KUA) used in this work was prepared by chemical activation of Spanish anthracite using KOH (Merck KGaA, Germany). The impregnation ratio of KOH to carbon precursor was set at 4:1. The activation was performed at 750 °C (heating rate: 5°/min, holding time: 1 h) in a tubular furnace (CTF12 & TZF12, Carbolite Gero Ltd., UK) under inert N_2 atmosphere (Air Liquide, France) with a flow rate of 800 mL/min. Subsequently, the mixture was stirred three times

for 1 h with 500 mL of 5 M HCl (Fisher Scientific, Spain), followed by three consecutive rinses with distilled water for 1 h to achieve neutral pH. The KUA material was recovered by filtration and dried at 120 °C. More details about the preparation and optimization of KUA preparation can be found elsewhere [33–35].

After preparation, the KUA material was ground in a ball mill (50 mL milling ZrO_2 container, MM 500 Nano, Retsch), using a 25 Hz crushing frequency for 15 min, to prepare fine KUA (KUA—F). This step was necessary due to the large size of the pristine KUA particles and the inability of its slurry electrode to flow in desalination experiments, even at a concentration as low as 5 wt%.

2.2.2. Oxidation of PAC activated carbon

PAC material was oxidized by a mild oxidation method using nitric acid to minimize the morphological changes and variation in the specific surface area of the PAC carbon. 1.5 g of PAC was added into 20 mL of 0.5 M HNO_3 solution and stirred for 3 h at room temperature. Then, it was filtered using a 0.2 μm polyether sulfone (PES) membrane and thoroughly washed with deionized water until the pH of the washing water equalled the deionized water. The obtained filter cake was dried in an oven at 100 °C for 2 h and then stored in an airtight container [19].

2.3. Physical characterization

AC powders were scanned using a JEOL JSM 7001F scanning electron microscope (SEM) to analyse their morphology. An Au/Pd thin film was sputtered onto the samples using a Q150T ES apparatus (Quorum Technologies) prior to that. Also, energy dispersive spectroscopy (EDS) with a light element detector (Oxford, model INCA 250) for semi-quantitative element identification was used to examine PAC and PAC-OX to verify the oxidation. The porous texture of all the tested ACs was determined by physical adsorption-desorption of N_2 at 77 K in a liquid nitrogen bath, and this was done using Micromeritics equipment, model ASAP 2010. For this analysis, the samples were outgassed at 150 °C under vacuum for at least 8 h. The specific surface area of the AC particles was determined by the Brunauer–Emmett–Teller (BET) method. The micropore volume of activated carbon materials was evaluated using the t-plot method. The average particle size and distribution of ACs were measured by laser scattering particle size distribution analyzer LA-960, HORIBA, Japan. The surface charge of ACs was assessed by measuring their zeta potential (ZP) in an aqueous medium (deionized water pH = 6.5) with a ZetaSizer Nano ZS particle size analyzer (Malvern Instruments, ZS 90, UK). The data was collected and analysed using the ZetaSizer Software 7.1 that integrates the device.

2.4. Rheological characterization

The rheology of carbon slurries was characterized using a coaxial cylinder (Rotor CC25 DIN Ti) in a controlled stress rheometer (Thermo Scientific, HAAKE MARS III, Germany) equipped with a Peltier heating system. Viscosity values were recorded as a function of shear rate, ranging from 1 to 215 s^{-1}, at a constant temperature of 20 °C.

2.5. Electrochemical characterization

2.5.1. Specific capacitance

The specific capacitance of carbon slurry electrodes was investigated using a symmetric two electrode electrochemical cell with platinum-coated titanium current collectors (210 mm length x 60 mm width). This cell was created by modifying an electrodialysis stack manufactured by MEGA in the Czech Republic [36]. Fig. 1 shows the schematic of this cell, while the specific details of the actual cell can be found in Fig. S1 of the Supporting Information. Slurries containing 20 wt% carbon were prepared in a 1 M NaCl electrolyte and stirred for 24 h in order to achieve homogeneity. The slurries were injected using a syringe into cell channels defined by rubber gaskets. The dimensions of each channel were: length = 150 mm, width = 2 mm, and depth = 1 mm. A polyether sulfone (PES) membrane with a pore size of 10 nm (NADIR® UP010 P, Germany) was used as a separator between two slurry electrodes. Cyclic voltammetry was conducted using a Vertex 5 A potentiostat (Ivium Technologies, The Netherlands). The experiments were carried out at a scan rate of 2 mV/s, over a voltage range of 0–1 V, with a step size of 1 mV. Five cycles were performed for each measurement and average values are reported. From cyclic voltammetry, the specific gravimetric capacitance (C_{sp}) was determined using Eq. (1):

$$C_{sp} = \frac{1}{(\Delta V m \upsilon)} \int i dV, \tag{1}$$

where ΔV is the width of the voltage window (V), i is the current (mA), υ is the scan rate (mV/s) and m is the total mass of carbon (g) inside the electrochemical cell [37,38].

2.5.2. Maximum salt adsorption capacity

The maximum salt adsorption capacity (max-SAC) was measured in an isolated close cycle (ICC) mode of flow electrode capacitive deionization (Fig. 2). This configuration was selected to ensure that the carbon materials reached their saturation point. This is achieved by having both, the cathodic and anodic flow electrodes operating in a closed cycle, and continuously charging them until all the carbon material in the flow electrode saturates. The same electrodialysis stack (MEGA, Czech Republic) was used to create an isolated close cycle flow electrode capacitive deionization (ICC-FCDI) cell (with one feed compartment and

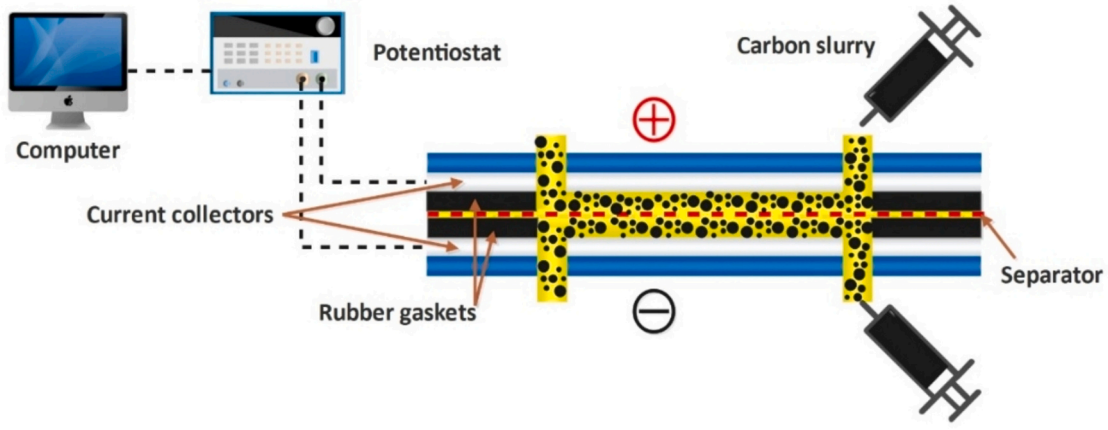

Fig. 1. Schematic representation of experimental set-up employed for measuring the specific capacitance.

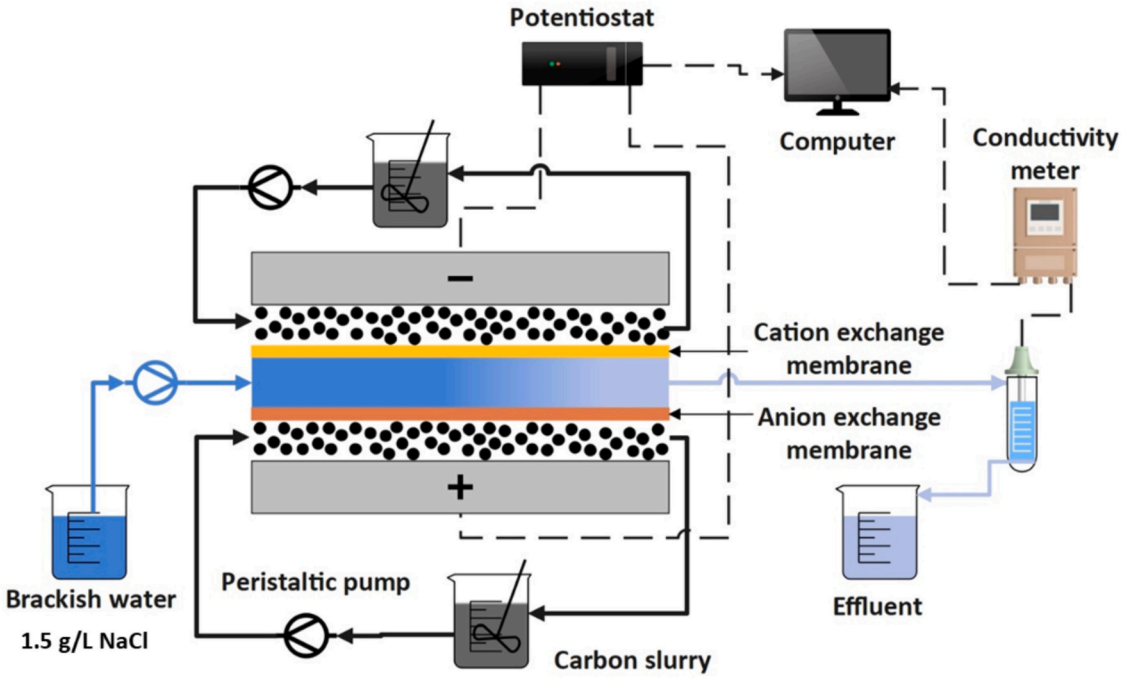

Fig. 2. Schematic illustration of isolated close cycle (ICC) mode of flow capacitive deionization experimental set-up employed for measuring the maximum salt adsorption capacity.

two flow electrode compartments) as reported in Section 2.5.1, but instead of a rubber gasket, 3D printed polyethylene terephthalate glycol (PET-G) gaskets were used to provide the path for the flow of carbon slurry. The details of flow electrode channel design and the 3D printing of gaskets can be seen in our previous study [39]. The assembly details of the FCDI cell with 3D-printed gaskets can be seen in Fig. S2 in the Supporting Information. A Fumasep® FAB-PK-130 anion-exchange membrane was placed between the feed channel and the anode compartment, and a Fumasep® FKB-PK-130 cation-exchange membrane was placed between the feed channel and the cathode compartment. Ion exchange membranes and the feed channel were 150 μm and 0.8 mm thick, respectively. The picture of the employed ICC-FCDI set-up is shown in Fig. S3 in the Supporting Information.

In this study, a 1.5 g/L solution of NaCl was used as the feed, which was introduced into the middle channel of the flow capacitive deionization (FCDI) cell at a flow rate of 10 mL/min using a peristaltic pump (Lead Fluid – BT100S, China). Carbon slurries, with a load of 5 wt% in a 1 g/L NaCl electrolyte, were prepared for these experiments. The flow electrodes, consisting of 50 mL of cathodic and anodic suspensions, were circulated at a flow rate of 60 mL/min *via* a peristaltic pump (Masterflex® L/S® Digital Peristaltic Pump Drive, UK). A constant potential difference of 1.2 V was applied using a Vertex 5 A potentiostat (Ivium Technologies, The Netherlands). The current generated within the FCDI cell, resulting from ion movements from the feed stream to the flow electrodes, was recorded. The conductivity of the effluent was measured at the outlet of the FCDI cell every 2 s using a conductivity meter (Horiba Laqua-PC1100, Japan). The experiments were conducted until the effluent stream conductivity matched that of the feed stream, indicating that the carbon electrodes had reached their saturation point and could no longer adsorb more salt. Maximum salt adsorption capacity (max-SAC) (mg of salt per gram of carbon at both electrodes) was calculated using the following Eqs. [39]:

$$\Gamma_{max} = \int_0^{t,charge} Q(c,feed - c,effluent)dt, \tag{2}$$

$$max - SAC = \Gamma_{max} * M\_salt / m\_electrodes, \tag{3}$$

where Γmax is the cumulative salt removed (mol), Q is the feedwater flow rate (L/s), c is the concentration (M), t is the time (s), M_salt is the molar mass of salt (58.44 g/mol) and m_electrodes is the total mass of active carbon material in both electrodes (g).

2.6. Desalination experiments

A single-cycle with separate concentrate chamber (SCSC) FCDI cell configuration (Fig. 3) was used in desalination experiments. A continuous flow of the AC suspension allows for simultaneous desalination and electrode regeneration within the same system, enabling efficient and continuous desalination operation [40]. A 1.5 g/L NaCl salt solution was used as synthetic brackish water feed. Flow electrodes with 5 wt%, 10 wt % and 15 wt% of ACs dispersed in 1 g/L NaCl aqueous solution were prepared. The volume of carbon slurry for each experiment was 100 mL and circulated through the FCDI cell at a flow rate of 60 mL/min. The flow rates of the concentrate and dilute streams were 1 mL/min. Each desalination experiment was performed for 1 h, during which a constant voltage of 1.0 V was applied using a Vertex 5 A potentiostat (Ivium Technologies, The Netherlands). The conductivity and pH of dilute and concentrate streams were recorded every 2 s using a conductivity/pH multimeter (Horiba Laqua-PC1100, Japan). The associated error with the conductivity measurements was ±0.5 %. The conductivity values were converted into NaCl concentration using the calibration curve reported in the Supporting Information (Fig. S4).

The desalination efficiency was calculated as follows [41]:

$$Desalination\ efficiency\ (\%) = \frac{(C_{feed,D} - C_{dilute})}{C_{feed,D}} \cdot 100, \tag{4}$$

where $C_{feed,D}$ is the feed NaCl concentration (g/L) and C_{dilute} is the effluent NaCl concentration in the dilute stream (g/L).

Current efficiency (CE), which relates the amount of transferred salt with the required electric current, was calculated at 1 h after the FCDI system reached its steady state. Current efficiency.

was determined as follows [8]:

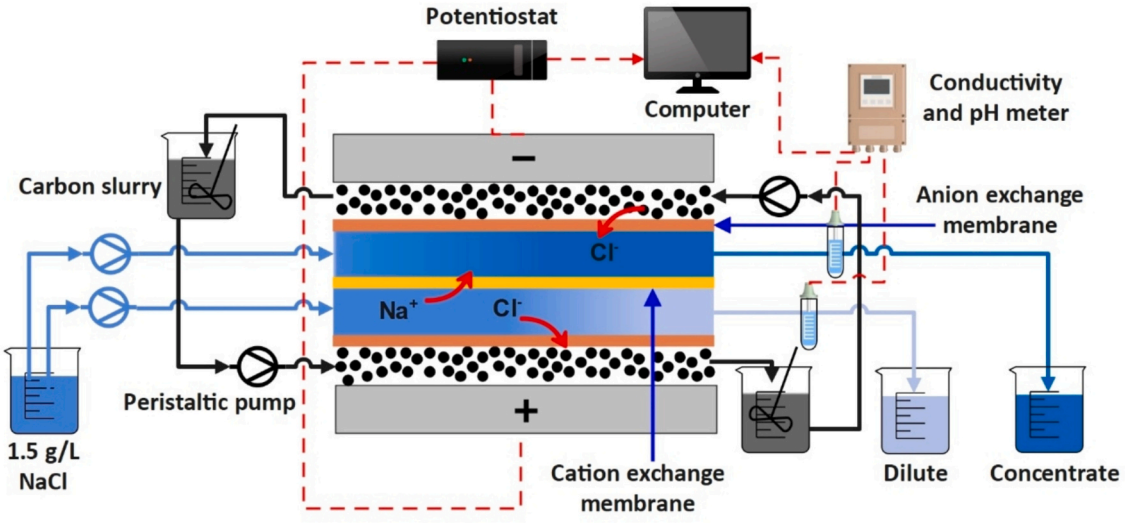

Fig. 3. The schematic diagram of the FCDI set-up used in desalination experiments.

$$CE\ (\%) = \frac{F.\dot{V}_{dilute}\left(C_{feed.D} - C_{dilute}\right)}{I.M_{NaCl}} \cdot 100, \quad (5)$$

where F is the Faraday constant 96,485 (C/mol), $\dot{V}_{dilute}$ is the volumetric flowrate of dilute (L/s), I is the current (A) and M_{NaCl} is the molar mass of NaCl (58.44 g/mol).

Specific energy consumption (Wh/mol) at 1 h of FCDI operation was calculated using eq. 6 [42]:

$$SEC = \frac{E.J.A.M_{NaCl}}{\left(C_{feed.D} - C_{diluted}\right).\dot{V}_{diluted.3600}}, \quad (6)$$

where E is the applied voltage (V), J is the current density (A/m^2), A is the effective contact area between the flow electrode and IEM (m^2), and 3600 is the unit conversion factor.

3. Results and discussion

3.1. Morphological characterization

The YP80F and YP50F carbon materials (Fig. 4a and b) have a finely textured composition consisting of small particles that are relatively uniform in size. This observation was further confirmed by measuring the particle size distribution of these carbons (Fig. 5), which was between 2 and 20 μm, representing the narrowest size distribution among all tested carbons. The Norit carbon (Fig. 4c) consists of larger and more irregularly shaped particles, some of which form aggregates. Furthermore, this carbon exhibited a bimodal particle size distribution where the first peak represents the average particle size of 10 μm while the second one depicts an average size of around 90 μm (Fig. 5). This bimodal particle size distribution might be helpful to lower the viscosity of Norit's slurry, as this fact has previously been reported [43]. The PAC and PAC-OX carbons (Fig. 4d-e) show similar heterogeneous morphology consisting of small granules and larger, random fragments. The surface modification (oxidation) of PAC to obtain PAC-OX does not significantly alter the particle size distribution (Fig. 5), as desired, since a mild oxidation method was performed. This will help assess the desalination performance variation only caused by surface chemistry modification and not by size reduction or size distribution variations.

Regarding the lab-made KUA and KUA-F materials, the SEM images show clear morphological differences (Fig. 4f and g) compared with the commercially available ACs (YP80F, YP50F, Norit, and PAC). The SEM image of pristine KUA (Fig. 4f) shows a heterogeneous surface with irregularly shaped particles, sharp edges, and varying sizes. The presence of larger particles might hinder the ability of the material to flow

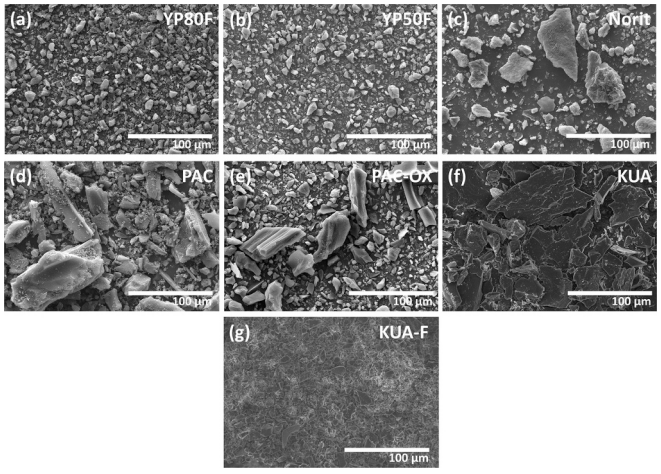

Fig. 4. Scanning electron microscope (SEM) top view images at 500× magnification of (a) YP80F, (b) YP50F, (c) Norit, (d) PAC and (e) PAC-OX (f) pristine KUA (g) KUA-F after 15 min of ball milling.

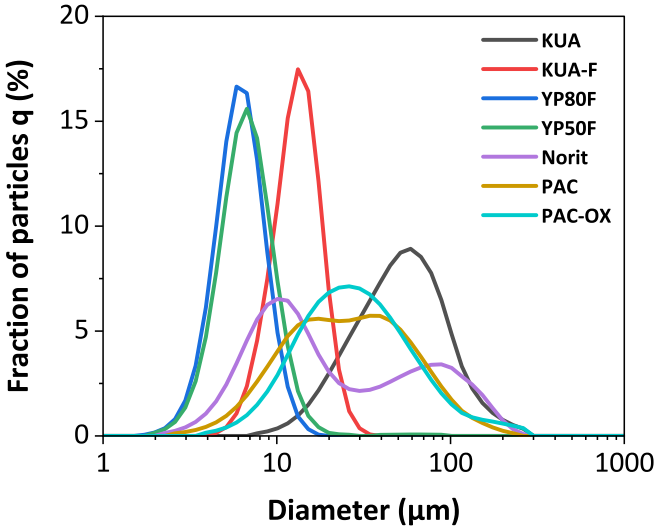

Fig. 5. Particle size distribution of activated carbons.

smoothly in an electrode slurry, potentially resulting in the occurrence of channelling effects or the blockage of channels, as indeed it was observed in the case of pristine KUA. Therefore, grinding was necessary to ensure the flowability of KUA slurry. After 15 min of ball milling, the KUA shows an important decrease in the mean particle size from 56.84 ± 0.10 μm to 12.70 ± 0.04 μm for KUA—F, with a significantly narrower size distribution (Fig. 5). The smaller particle size, smoother surface, and reduced number of sharp edges (Fig. 4g) improved particle contact and increased accessibility of the surface area, which could potentially have a positive impact on the desalination performance. The SEM images of all the analysed carbons at higher magnifications (5000× and 10,000×) can be seen in Fig. S5 of the Supporting Information.

An Energy Dispersive Spectroscopy (EDS) analysis was also performed on PAC and PAC-OX samples to evaluate their atomic composition, specifically focusing on the oxygen atom to verify the oxidation of PAC. The analysis covered a large representative area (Fig. S6 and Table S1 in the Supplementary Information). The elemental analyses show higher oxygen content in PAC-OX (18 %) compared to PAC (11 %), thus confirming the oxidation of the PAC sample.

3.2. Specific capacitance and salt adsorption capacity

The specific capacitance (Fig. 6a-b) and maximum salt adsorption capacity (Fig. 6c-d) of ACs were measured to assess their electrochemical performance in FCDI. The cyclic voltammograms (CV) of all carbon materials exhibited a quasi-rectangular shape although, in some cases, the CV are tilted due to higher resistance. These CV confirm the efficient capacitive charge transfer between the carbon flow electrode and the platinum coated titanium current collectors.

KUA-F exhibited the highest specific capacitance of 55 F/g among the tested materials, a remarkable 38 times increase compared to the pristine KUA, which only had a specific capacitance of 1.5 F/g. As confirmed by the SEM analysis, the milling process is responsible for this substantial improvement, as it reduced the particle size and improved the uniformity of the carbon particles. It is also interesting to note that the specific surface area of KUA (2800 m^2/g) after milling did not change significantly (KUA-F = 2817 m^2/g), thus the milling process did not significantly affect the KUA internal structure in terms of mesopores and nanopores as the slight increase in S_{BET} is just due to the increase associated with the creation of smaller particles. This means that the access of nitrogen to the internal surface of the material is basically the same, but the wetting by the electrolyte and diffusion of ions into adsorption sites is facilitated by the shorter diffusion paths. Thus, the smaller particle of KUA-F is an important factor for the observed improvement in electrochemical performance as it increases the surface area accessibility and promotes better particle-particle contact that decreases the resistance for charge percolation. Additionally, KUA-F has a maximum salt adsorption capacity of 185 mg/g, which is 26 % higher than that of YP80F, a commercially available AC known for its high performance.

YP80F showed superior electrochemical performance compared to YP50F, with a specific capacitance of 44 F/g against 9 F/g, respectively. Despite their comparable morphologies, the substantial difference in specific capacitance, an increase of approximately five-fold for YP80F, can be attributed to their specific surface areas. YP80F has a significantly higher S_{BET} of 2226 m^2/g than YP50F, which has 1606 m^2/g. The increased surface area means greater availability of active sites and micropores for the adsorption of ions, resulting in enhanced electrochemical performance [44]. YP80F exhibited a notable salt adsorption capacity of 147 mg/g, surpassing YP50F's capacity of 122 mg/g by 21 %, further highlighting the influence of surface area on salt removal performance [45].

The Norit AC, with a 750 m^2/g surface area, exhibited a specific capacitance of 6 F/g and a maximum salt adsorption capacity of 66 mg/g. The inferior performance of Norit, which exhibits a specific capacitance approximately 6.5 % lower than that of YP50F, can be attributed to its larger and more irregular particle morphology with reduced surface area and inefficient ion transport caused by larger particle size. This observation is in agreement with previous studies that have associated similar morphological characteristics with decreased capacitance [46]. Despite the relatively high S_{BET} values of 1454 m^2/g for PAC and 1325 m^2/g for PAC-OX, their specific capacitances were 0.9 F/g and 0.7 F/g, respectively. The oxidation process in PAC-OX, validated by EDS-SEM through the analysis of oxygen content, adversely affected the material specific surface area due to the introduction of oxygen-containing functional groups (such as carboxyl, hydroxyl, and carbonyl groups)

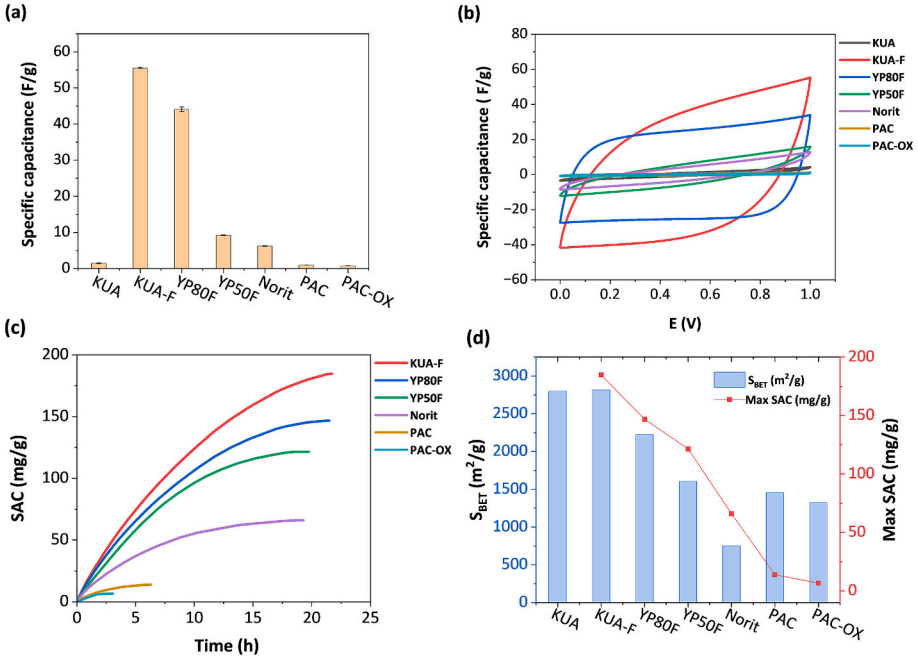

Fig. 6. (a) Specific capacitance, (b) cyclic voltammograms at a scan rate of 2 mV/s, (c) salt adsorption capacity over time and (d) maximum salt adsorption capacity and specific surface area of all the tested activated carbons (except Max SAC for KUA since it did not flow).

on the surface of AC. These groups can partially block the pores, especially micropores, substantially affecting the specific surface area [47]. Furthermore, their inadequate performance is likely due to larger fragment sizes and irregular morphology, which can impede efficient ion transport and diminish the effective surface area available for charge storage. This is reflected in their low salt adsorption capacities of 14 mg/g for PAC and 7 mg/g for PAC-OX.

Another important factor that might influence the electrochemical and ion adsorption performance of activated carbons is the balance between micropore and mesopore volumes. While the accessibility of active sites is enhanced by smaller particle sizes and higher specific surface areas, the pores' structure affects ion transport and storage. Mesopores serve as transport pathways, with reduced resistance, enabling faster access of ions to the micropores, which are the primary sites for ion adsorption and charge storage [48]. The mesopore volume of KUA-F was found to be 0.15 cm^3/g, which is higher than that of KUA (0.10 cm^3/g) as shown in Table 1. The synergistic effect of having higher mesoporosity, promoting easy access to the active sites, and smaller particle size could be the reason for the exceptional specific capacitance (55 F/g) and salt adsorption capacity (185 mg/g) for KUA-F in comparison to KUA.

Additionally, this interplay between micro and mesopores is highlighted by the performance comparison with other activated carbons. For example, Norit and PAC exhibit higher mesopore volumes (0.51 and 0.53 cm^3/g, respectively) but lower micropore volumes (0.18 and 0.07 cm^3/g, respectively), which leads to suboptimal adsorption and capacitance. This emphasizes the importance of maintaining a balance between the volumes of micropores and mesopores [49]. YP80F's specific capacitance of 44 F/g is further validated by its moderate mesopore volume (0.20 cm^3/g) and substantial micropore volume (0.96 cm^3/g), which demonstrate the impact of pore accessibility in achieving high performance. So, the enhanced electrochemical performance of KUA-F is not only due to the smaller particle size and higher specific surface area but also results from an optimised mesopore to micropore ratio.

3.3. Rheological properties of activated carbon slurries

The viscosity of all carbon slurries decreased as the shear rate increased, indicating that they exhibited a shear-thinning behaviour (Fig. S7 in the Supporting Information). This behaviour can be explored in flow electrode applications to reduce the energy required to pump the slurry through the system by smartly decreasing its viscosity [19]. The behaviour of shear thinning systems can be modelled using the Ostwald-de Waele power law, described by eq. (7):

$$\eta = \kappa \cdot \dot{\gamma}^{n-1}, \tag{7}$$

where η (Pa.s) is the effective viscosity, κ ($Pa \cdot s^n$) is the consistency index, $\dot{\gamma}$ (s^{-1}) is the shear rate, and n (dimensionless) is the shear thinning index.

The parameter n represents the degree of shear-thinning, where smaller values indicate a higher level of shear-thinning, and $n = 1$ corresponds to a Newtonian fluid [50,51]. The viscosity curves in relation to shear rate and their corresponding fitting parameters can be found in Fig. S7 and Table S2 of the Supporting Information. The viscosity of the carbon slurries increases with the increase of the weight percentage of ACs, as depicted in Fig. 7a. YP80F and KUA-F demonstrated the highest viscosities among the tested slurries, specifically at higher solid loadings of 20 wt%, with values of 0.4477 Pa·s and 0.4475 Pa·s at a shear rate of 215 s^{-1}, respectively. This increased viscosity is due to the finer particle size distribution and increased surface area, which lead to extensive particle-particle interactions and a more cohesive slurry structure [52]. The significant negative zeta potential values observed for YP80F (−27.25 mV) and KUA-F (−34.60 mV) are in agreement with the higher viscosity, indicating stronger electrostatic repulsion between particles (Fig. 7b). This repulsion contributes to maintain a stable dispersion, thereby reducing the tendency for aggregation and resulting in the higher viscosity observed at these concentrations.

KUA-F (finely milled in a ball mill) has a higher viscosity than pristine KUA, especially at 20 wt% of carbon loading. Decreasing the particle size increases the number of particles and surface area, thereby increasing the number of interaction sites. This results in a denser network of particles within the slurry. The densification is reflected in the zeta potential values, with KUA-F exhibiting a considerably more negative potential (−34.60 mV) than KUA (−7.34 mV). The higher negative zeta potential of KUA-F indicates a greater level of stability in suspension, which is likely responsible for its increased viscosity by ensuring the dispersion of particles and preventing settling.

YP80F, although sharing a similar morphology with YP50F, exhibits significantly greater viscosity. The larger surface area of YP80F is likely to enhance the potential for interparticle interactions, consequently raising the resistance to flow, a phenomenon already reported in the literature [50]. The zeta potential values further confirm this observation, as YP80F demonstrates a more pronounced negative potential (−27.25 mV) compared to YP50F (−24.65 mV), suggesting a more stable suspension with reduced particle aggregation. In contrast, Norit and PAC slurries, characterized by reduced specific surface areas and increased particle sizes, demonstrated lower viscosities at a concentration of 20 wt% (0.1139 Pa·s and 0.3437 Pa·s at a shear rate of 215 s^{-1}, respectively). Furthermore, they exhibited a broader range of particle size distribution (Fig. 5) compared to other activated carbons, which may account for the lower viscosity. It is a known fact that an increase in particle size distribution leads to a decrease in viscosity [53]. In addition, Norit exhibits a lower zeta potential of −0.85 mV, indicating a reduced level of electrostatic stabilization and an increased probability of particle aggregation.

The slurry of PAC-OX exhibits a lower viscosity at a shear rate of 215 s^{-1} (0.0959 Pa·s at 20 wt%) than its original counterpart. This reduction in viscosity can be attributed to the oxidation process, which increased the oxygen functional groups on the surface (as confirmed by EDS-SEM analysis) by reducing the hydrophobic interactions between carbon particles and increasing the surface's hydrophilicity and particle solvation [19]. Furthermore, the zeta potential of PAC-OX (−29.30 mV) is slightly less negative than that of PAC (−30.30 mV), suggesting a marginally reduced electrostatic repulsion that could contribute to the lower viscosity by enabling particles to come closer together, thereby reducing the resistance to flow. In general, the rheological properties of these carbon slurries are connected to their zeta potential, surface area, and particle size. The data indicates that higher viscosities, which are accompanied by more negative zeta potentials, are associated with improved suspension stability and interparticle interactions. These properties are essential for optimizing the performance of carbon slurries in FCDI applications.

Table 1
The pore volume of activated carbon samples.

Activated carbon	V_{tot} (cm^3/g)	V_{micro} (cm^3/g)	V_{meso} (cm^3/g)
KUA	1.41	1.31	0.10
KUA-F	1.44	1.29	0.15
YP80F	1.16	0.96	0.20
YP50F	0.73	0.61	0.12
Norit	0.69	0.18	0.51
PAC	0.60	0.07	0.53
PAC-OX	0.54	0.09	0.45

3.4. Desalination performance

The chronoamperometric curves of all the tested carbons are shown in Fig. 8a-c. YP80F shows the highest current response compared to other commercial tested counterparts (YP50F, Norit and PAC), indicating its higher capacity for salt removal. The observed higher current values could be due to its highest specific surface area and smaller

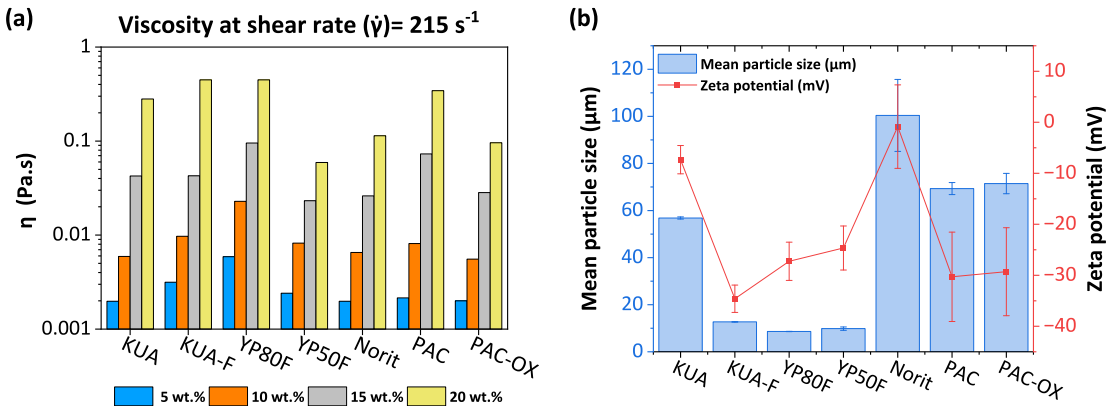

Fig. 7. (a) Viscosity of activated carbon at the shear rate of 215 s^{-1}, (b) Mean particle size and zeta potential of activated carbons.

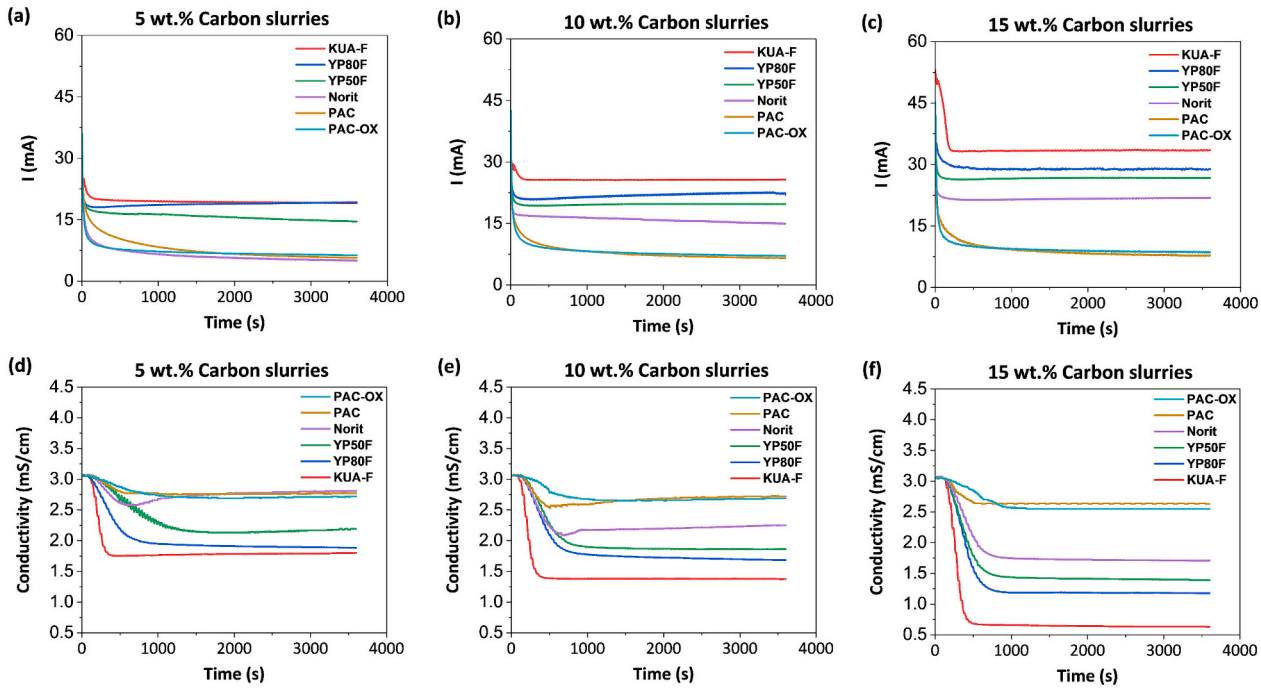

Fig. 8. Chronoamperometric curves and dilute stream conductivity for FCDI stacks using different carbon materials in flow electrodes at (a, d) 5 wt%, (b, e) 10 wt%, and (c, f) 15 wt% of carbon loadings during desalination of a 1.5 g/L NaCl solution mimicking brackish water.

particle size among the tested commercial ACs, which enhanced the particle-particle interaction and facilitated the charge transfer. All other commercial ACs follow the same trend of a higher specific surface area corresponding to a higher current response in FCDI (YP50F > Norit > PAC). A general trend between AC loading and current response was also observed; the higher the AC loading, the higher the registered current in the FCDI cell, regardless of the type of AC used in the flow electrodes.

On the other hand, the fine form of the lab-made AC, KUA—F, exhibited the highest current response compared to all the tested carbons, including YP80F, which showed the highest current values among the commercial ACs. This observation indicates KUA-F's superior salt removal capability. At a loading of 15 wt%, KUA-F demonstrated a consistently high and stable current during the desalination process, surpassing the other carbons by a significant margin. For example, when KUA-F was used as a flow electrode, 1.2 and 3.9 times higher current was recorded compared to YP80F and PAC-OX, respectively. This pattern persisted regardless of the carbon loading, demonstrating KUA-F's robust performance in the FCDI setup.

Higher recorded currents during the FCDI process correlate with higher salt removal, as evidenced by the corresponding decrease in the dilute stream conductivity (Fig. 8d-f). The faster drop in dilute conductivity and consistently lower values across all carbon loadings when KUA-F was used as the flow electrode confirm the increased salt removal and are in direct correlation with the higher currents measured. The enhanced desalination performance was particularly evident at higher loadings (10 wt% and 15 wt%), where KUA-F showed a 20–30 % higher decrease in conductivity compared to YP80F. This emphasizes the potential of KUA-F as a superior substitute for commercial ACs in FCDI applications.

The oxidation of PAC to PAC-OX did not result in a substantial enhancement of desalination performance. It only led to a slight (2 %) improvement in desalination efficiency, as shown in Fig. 9c. Thus, the overall performance of PAC and PAC-OX remained inferior to the other tested carbons. This result highlights how crucial it is to optimize not only the surface chemistry but also the particle size, morphology and accessible surface area to attain optimal desalination performance. The stability of the FCDI system was also evaluated by monitoring the pH of the dilute stream. The pH of the treated water remains relatively stable,

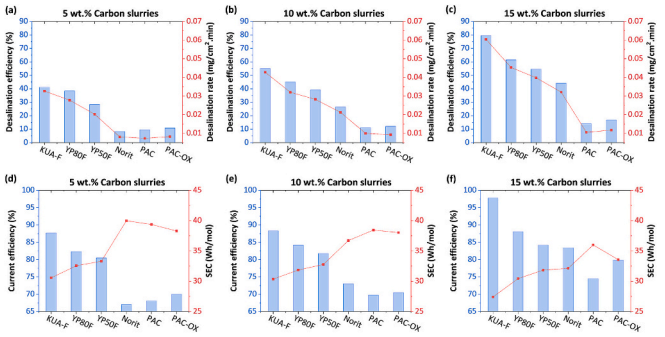

Fig. 9. Desalination efficiency and rate (a-c) and current efficiency and specific energy consumption (SEC) (d-f) at 5 wt%, 10 wt% and 15 wt% activated carbon loadings during desalination of a 1.5 g/L NaCl solution mimicking brackish water.

with minor fluctuations across all tested carbon materials. This suggests that in the tested FCDI configuration, the desalination process has a minimal impact on the pH of the treated water, thus ensuring the desired quality (Fig. S8 in the Supporting Information).

Building on these findings, the desalination efficiency and rate further demonstrated the superiority of KUA—F, which consistently outperformed commercial carbons across different loading levels. Fig. 9a-c shows that the differences in desalination efficiency and rate are more evident when higher carbon loadings are used in flow electrodes. KUA-F (at 15 wt% loading) achieved a desalination efficiency of 79 %, surpassing YP80F by 29 %, YP50F by 46 %, and Norit by 80 %. This trend is mirrored in the desalination rate, where KUA-F exhibited a rate of 0.06 mg/cm^2.min, outperforming YP80F by 33 %, YP50F by 52 % and Norit by 88 %. Although the improved desalination rate and efficiency indicate KUA-F better ion removal performance, it is also essential to consider the current efficiency and energy consumption, in order to fully understand its effectiveness.

KUA-F achieved a current efficiency of 98 % at 15 wt% of its loading in the flow electrode, which is 11 % higher than YP80F, 16 % higher than YP50F, and 17 % higher than Norit. This is accompanied by a decrease in specific energy consumption to 27 Wh/mol, which represents a 10 % drop compared to YP80F, 14 % less compared to YP50F, and 15 % less compared to Norit. These findings highlight superior KUA-F energy efficiency in FCDI applications.

4. Conclusions

This study systematically evaluated the desalination performance of flow electrode capacitive deionization (FCDI) using flow electrodes prepared from both commercial (YP80F, YP50F, Norit, PAC) and lab-made (KUA, KUA—F, PAC-OX) activated carbons (ACs). Among the tested materials, lab-made KUA—F, characterized by a high specific surface area, small particle size, narrow size distribution, high volume of micropores and superior specific capacitance, demonstrated the most efficient desalination performance. In contrast, despite its high surface area (~2800 m^2/g), pristine KUA lacked flowability due to its larger particle size and broad distribution. Improvement in desalination performance was observed with increased carbon loading in flow electrodes for all activated carbons. The performance differences become more prominent at higher loadings (15 wt%). Surface oxidation of PAC (PAC-OX) introduced oxygen functional groups but yielded only marginal improvements (~2 %) in efficiency, likely due to its larger particle size and broader distribution. Therefore, effective FCDI flow electrode materials require a high specific surface area, small particle size (1–10 μm), optimised ratio of micro and mesopores, hydrophilic surface chemistry for easy dispersion in aqueous electrolytes, and excellent electrochemical properties like high specific capacitance. The optimised morphological and electrochemical properties of KUA-F significantly improved desalination efficiency and energy savings, underscoring its potential for scalable FCDI applications. Future work should focus on scaling KUA-F production and exploring its broader applicability in electrochemical processes.

Declaration of competing interest

The authors declare that they have no known competing financial interests or personal relationships that could have appeared to influence the work reported in this paper.

Acknowledgements

This work received funding from Fundação para a Ciência e Tecnologia, I.P. (FCDT/MCTES) under grant agreement No PTDC/EQU-EQU/6193/2020 (Se(*L*)ect(i)vity). This work received funding from the European Union Horizon 2020 research and innovation programme under grant agreement No 869467 (SEArcularMINE). This work was also supported by the Associate Laboratory for Green Chemistry – LAQV and LEAF research centres, financed by national Portuguese funds from FCT/MCTES (UIDB/50006/2020 and UIDB/04129/2020, respectively). This work was also funded by grant PLEC2023-010216 funded by MICIU/AEI/10.13039/501100011033. Hafiz Muhammad Saif Ullah Saleem acknowledges FCT/MCTES for his PhD grant 2020.09828.BD (https://doi.org/10.54499/2020.09828.BD). B. Ferrández-Gómez acknowledges the University of Alicante for his mobility grant (UA_movilidad 2020).

Appendix A. Supplementary data

Supplementary data to this article can be found online at https://doi.org/10.1016/j.desal.2025.118638.

References

[1] W. Xing, J. Liang, W. Tang, D. He, M. Yan, X. Wang, Y. Luo, N. Tang, M. Huang, Versatile applications of capacitive deionization (CDI)-based technologies, Desalination 482 (2020) 114390, https://doi.org/10.1016/j.desal.2020.114390.
[2] M.A. Luciano, H. Ribeiro, G.E. Bruch, G.G. Silva, Efficiency of capacitive deionization using carbon materials based electrodes for water desalination, J. Electroanal. Chem. 859 (2020) 113840, https://doi.org/10.1016/j.jelechem.2020.113840.
[3] S. Il Jeon, H.R. Park, J.G. Yeo, S. Yang, C.H. Cho, M.H. Han, D.K. Kim, Desalination via a new membrane capacitive deionization process utilizing flow-electrodes, energy, Environ. Sci. 6 (2013) 1471–1475, https://doi.org/10.1039/c3ee24443a.
[4] H.J. Chung, J. Kim, D.I. Kim, G. Gwak, S. Hong, Feasibility study of reverse osmosis–flow capacitive deionization (RO-FCDI) for energy-efficient desalination using seawater as the flow-electrode aqueous electrolyte, Desalination 479 (2020) 114326, https://doi.org/10.1016/j.desal.2020.114326.
[5] Y.U. Shin, J. Lim, C. Boo, S. Hong, Improving the feasibility and applicability of flow-electrode capacitive deionization (FCDI): review of process optimization and energy efficiency, Desalination 502 (2021) 114930, https://doi.org/10.1016/j.desal.2021.114930.
[6] Y. Gendel, A.K.E. Rommerskirchen, O. David, M. Wessling, Batch mode and continuous desalination of water using flowing carbon deionization (FCDI) technology, Electrochem. Commun. 46 (2014) 152–156, https://doi.org/10.1016/j.elecom.2014.06.004.
[7] S. Porada, D. Weingarth, H.V.M. Hamelers, M. Bryjak, V. Presser, P.M. Biesheuvel, Carbon flow electrodes for continuous operation of capacitive deionization and capacitive mixing energy generation, J. Mater. Chem. A Mater. 2 (2014) 9313–9321, https://doi.org/10.1039/c4ta01783h.
[8] A. Rommerskirchen, C.J. Linnartz, F. Egidi, S. Kendir, M. Wessling, Flow-electrode capacitive deionization enables continuous and energy-efficient brine concentration, Desalination 490 (2020) 114453, https://doi.org/10.1016/j.desal.2020.114453.
[9] J. Ma, J. Ma, C. Zhang, J. Song, W. Dong, T.D. Waite, Flow-electrode capacitive deionization (FCDI) scale-up using a membrane stack configuration, Water Res. 168 (2020) 115186, https://doi.org/10.1016/j.watres.2019.115186.
[10] J. Ma, X. Wang, R. Zhou, J. Chen, L. Rao, L. Zheng, F. Yu, Flow-electrode capacitive deionization (FCDI): selective recovery applications and expanded structural design, Desalination 599 (2025) 118455, https://doi.org/10.1016/j.desal.2024.118455.
[11] X. Wang, F. Qi, S. Wang, P. Zhu, X. Wei, Z. Li, J. Zhao, Simultaneous desalination and removal of organic pollutants in a novel bifunctional FCDI system: the enhancement by in-situ reutilization of chloride ions, Desalination 592 (2024) 118107, https://doi.org/10.1016/j.desal.2024.118107.

[12] Y. He, X. Zhang, K. Zuo, F. Yang, T. Gao, P. Liang, Highly efficient and selective extraction of phosphorous from wastewater as vivianite in a strategically operated four-chamber flow electrode capacitive deionization, Desalination 544 (2022) 116089, https://doi.org/10.1016/j.desal.2022.116089.
[13] Z. Tang, Y. Li, K. Tan, G. Wang, C. Li, L. Liu, Z. Liu, Efficient removal of uranium and sulfate in acid contaminated groundwater by flow electrode capacitive deionization, Desalination 594 (2025) 118304, https://doi.org/10.1016/j.desal.2024.118304.
[14] G. Ma, J. Jiang, Y. Wei, A. Cai, L. Wang, H. Zhou, Lithium extraction from salt lake via rocking-chair flow electrode capacitive deionization with monovalent selective membrane, Desalination 600 (2025) 118516, https://doi.org/10.1016/j.desal.2024.118516.
[15] H.M. Saif, J.G. Crespo, S. Pawlowski, Lithium recovery from brines by lithium membrane flow capacitive deionization (Li-MFCDI) – a proof of concept, J. Membr. Sci. Lett. 3 (2023) 100059, https://doi.org/10.1016/j.memlet.2023.100059.
[16] M. Tauk, M. Bechelany, S. Lagerge, P. Sistat, R. Habchi, M. Cretin, F. Zaviska, Influence of particle size distribution on carbon-based flowable electrode viscosity and desalination efficiency in flow electrode capacitive deionization, Sep. Purif. Technol. 306 (2023) 122666, https://doi.org/10.1016/j.seppur.2022.122666.
[17] T. Eguchi, Y. Kanamoto, M. Tomioka, D. Tashima, S. Kumagai, Effect of ball milling on the electrochemical performance of activated carbon with a very high specific surface area, Batteries 6 (2020) 22, https://doi.org/10.3390/batteries6020022.
[18] G. Folaranmi, M. Tauk, M. Bechelany, P. Sistat, M. Cretin, F. Zaviska, Investigation of fine activated carbon as a viable flow electrode in capacitive deionization, Desalination 525 (2022) 115500, https://doi.org/10.1016/j.desal.2021.115500.
[19] K.B. Hatzell, M.C. Hatzell, K.M. Cook, M. Boota, G.M. Housel, A. McBride, E. C. Kumbur, Y. Gogotsi, Effect of oxidation of carbon material on suspension electrodes for flow electrode capacitive deionization, Environ. Sci. Technol. 49 (2015) 3040–3047, https://doi.org/10.1021/es5055989.
[20] J.W. Campos, M. Beidaghi, K.B. Hatzell, C.R. Dennison, B. Musci, V. Presser, E. C. Kumbur, Y. Gogotsi, Investigation of carbon materials for use as a flowable electrode in electrochemical flow capacitors, Electrochim. Acta 98 (2013) 123–130, https://doi.org/10.1016/j.electacta.2013.03.037.
[21] E. Botha, N. Smith, B. Hlabano-Moyo, B. Bladergroen, The effect of slurry wet mixing time, thermal treatment, and method of electrode preparation on membrane capacitive deionisation performance, Processes 9 (2021) 1–17, https://doi.org/10.3390/pr9010001.
[22] M.C. Hatzell, K.B. Hatzell, B.E. Logan, Using flow electrodes in multiple reactors in series for continuous energy generation from capacitive mixing, Environ. Sci. Technol. Lett. 1 (2014) 474–478, https://doi.org/10.1021/ez5003314.
[23] H.M. Saif, J.G. Crespo, S. Pawlowski, Can 3D-printed flow electrode gaskets replace CNC-milled graphite current collectors in flow capacitive deionization? Desalination 597 (2025) 118362 https://doi.org/10.1016/j.desal.2024.118362.
[24] J. Ma, C. Zhang, F. Yang, X. Zhang, M.E. Suss, X. Huang, P. Liang, Carbon black flow electrode enhanced electrochemical desalination using single-cycle operation, Environ. Sci. Technol. 54 (2020) 1177–1185, https://doi.org/10.1021/acs.est.9b04823.
[25] K. Tang, S. Yiacoumi, Y. Li, C. Tsouris, Enhanced water desalination by increasing the Electroconductivity of carbon powders for high-performance flow-electrode capacitive deionization, ACS Sustain. Chem. Eng. 7 (2019) 1085–1094, https://doi.org/10.1021/acssuschemeng.8b04746.
[26] P. Liang, X. Sun, Y. Bian, H. Zhang, X. Yang, Y. Jiang, P. Liu, X. Huang, Optimized desalination performance of high voltage flow-electrode capacitive deionization by adding carbon black in flow-electrode, Desalination 420 (2017) 63–69, https://doi.org/10.1016/j.desal.2017.05.023.
[27] S. Li, K. Han, J. Li, M. Li, C. Lu, Preparation and characterization of super activated carbon produced from gulfweed by KOH activation, Microporous Mesoporous Mater. 243 (2017) 291–300, https://doi.org/10.1016/j.micromeso.2017.02.052.
[28] Z. Zhang, Y. Zhang, C. Jiang, D. Li, Z. Zhang, K. Wang, W. Liu, X. Jiang, Y. Rao, C. Xu, X. Chen, N. Meng, Highly efficient capacitive desalination for brackish water using super activated carbon with ultra-high pore volume, Desalination 529 (2022) 115653, https://doi.org/10.1016/j.desal.2022.115653.
[29] Z. Zhang, Y. Lei, D. Li, J. Zhao, Y. Wang, G. Zhou, C. Yan, Q. He, Sudden heating of H3PO4-loaded coconut shell in CO2 flow to produce super activated carbon and its application for benzene adsorption, renew, Energy 153 (2020) 1091–1099, https://doi.org/10.1016/j.renene.2020.02.059.
[30] M. Sevilla, G.A. Ferrero, A.B. Fuertes, Beyond KOH activation for the synthesis of superactivated carbons from hydrochar, Carbon 114 (2017) 50–58, https://doi.org/10.1016/j.carbon.2016.12.010.
[31] A. Elmouwahidi, E. Bailón-García, A.F. Pérez-Cadenas, F.J. Maldonado-Hódar, F. Carrasco-Marín, Activated carbons from KOH and H3PO4-activation of olive residues and its application as supercapacitor electrodes, Electrochim. Acta 229 (2017) 219–228, https://doi.org/10.1016/j.electacta.2017.01.152.
[32] M.J.P. Brito, C.M. Veloso, L.S. Santos, R.C.F. Bonomo, R. da C.I. Fontan, Adsorption of the textile dye Dianix® royal blue CC onto carbons obtained from yellow mombin fruit stones and activated with KOH and H3PO4: kinetics, adsorption equilibrium and thermodynamic studies, Powder Technol. 339 (2018) 334–343, https://doi.org/10.1016/j.powtec.2018.08.017.
[33] A. Gabe, R. Ruiz-Rosas, C. González-Gaitán, E. Morallón, D. Cazorla-Amorós, Modeling of oxygen reduction reaction in porous carbon materials in alkaline medium, Effect of microporosity, J. Power Sources 412 (2019) 451–464, https://doi.org/10.1016/j.jpowsour.2018.11.075.
[34] M.J. Mostazo-López, J. Krummacher, A. Balducci, E. Morallón, D. Cazorla-Amorós, Electrochemical performance of N-doped superporous activated carbons in ionic liquid-based electrolytes, Electrochim. Acta 368 (2021) 137590, https://doi.org/10.1016/j.electacta.2020.137590.
[35] D. Lozano-Castello, M. Lillo-Rodenas, D. Cazorla-Amoros, A. Linares-Solanó, Preparation of activated carbons from Spanish anthracite I, Activation by KOH, Carbon 39 (2001) 741–749, https://doi.org/10.1016/S0008-6223(00)00185-8.
[36] S. Pawlowski, J.G. Crespo, S. Velizarov, Pressure drop in reverse electrodialysis: experimental and modeling studies for stacks with variable number of cell pairs, J. Membr. Sci. 462 (2014) 96–111, https://doi.org/10.1016/j.memsci.2014.03.020.
[37] B. Akuzum, L. Agartan, J. Locco, E.C. Kumbur, Effects of particle dispersion and slurry preparation protocol on electrochemical performance of capacitive flowable electrodes, J. Appl. Electrochem. 47 (2017) 369–380, https://doi.org/10.1007/s10800-017-1046-5.
[38] Y. Cai, X. Zhao, Y. Wang, D. Ma, S. Xu, Enhanced desalination performance utilizing sulfonated carbon nanotube in the flow-electrode capacitive deionization process, Sep. Purif. Technol. 237 (2020) 116381, https://doi.org/10.1016/j.seppur.2019.116381.
[39] H.M. Saif, T.H. Gebregeorgis, J.G. Crespo, S. Pawlowski, The influence of flow electrode channel design on flow capacitive deionization performance: experimental and CFD modelling insights, Desalination 578 (2024) 117452, https://doi.org/10.1016/j.desal.2024.117452.
[40] A. Rommerskirchen, Y. Gendel, M. Wessling, Single module flow-electrode capacitive deionization for continuous water desalination, Electrochem. Commun. 60 (2015) 34–37, https://doi.org/10.1016/j.elecom.2015.07.018.
[41] S. Yang, J. Choi, J.G. Yeo, S. Il Jeon, H.R. Park, D.K. Kim, Flow-electrode capacitive deionization using an aqueous electrolyte with a high salt concentration, Environ. Sci. Technol. 50 (2016) 5892–5899, https://doi.org/10.1021/acs.est.5b04640.
[42] C. Shi, H. Wang, A. Li, G. Zhu, X. Zhao, F. Wu, Process model for flow-electrode capacitive deionization for energy consumption estimation and system optimization, Water Res. 230 (2023) 119517, https://doi.org/10.1016/j.watres.2022.119517.
[43] R. Greenwood, P.F. Luckham, T. Gregory, Minimising the viscosity of concentrated dispersions by using bimodal particle size distributions, Colloids Surf. A Physicochem. Eng. Asp. 144 (1998) 139–147, https://doi.org/10.1016/S0927-7757(98)00409-9.
[44] M.E. Suss, S. Porada, X. Sun, P.M. Biesheuvel, J. Yoon, V. Presser, Water desalination via capacitive deionization: what is it and what can we expect from it?, energy, Environ. Sci. 8 (2015) 2296–2319, https://doi.org/10.1039/c5ee00519a.
[45] J. Zhang, T. Yan, J. Fang, J. Shen, L. Shi, D. Zhang, Enhanced capacitive deionization of saline water using N-doped rod-like porous carbon derived from dual-ligand metal-organic frameworks, environ Sci, Nano 7 (2020) 926–937, https://doi.org/10.1039/c9en01216h.
[46] X. Xu, L. Pan, Y. Liu, T. Lu, Z. Sun, Enhanced capacitive deionization performance of graphene by nitrogen doping, J. Colloid Interface Sci. 445 (2015) 143–150, https://doi.org/10.1016/j.jcis.2015.01.003.
[47] S.Y. Yang, B.C. Bai, Y.R. Kim, Effective surface structure changes and characteristics of activated carbon with the simple introduction of oxygen functional groups by using radiation energy, Surfaces 7 (2024) 12–25, https://doi.org/10.3390/surfaces7010002.
[48] Y. Wang, Y. Chen, H. Zhao, L. Li, D. Ju, C. Wang, B. An, Biomass-derived porous carbon with a good balance between high specific surface area and Mesopore volume for supercapacitors, Nanomaterials 12 (2022) 3804, https://doi.org/10.3390/nano12213804.
[49] C.L. Yeh, H.C. Hsi, K.C. Li, C.H. Hou, Improved performance in capacitive deionization of activated carbon electrodes with a tunable mesopore and micropore ratio, Desalination 367 (2015) 60–68, https://doi.org/10.1016/j.desal.2015.03.035.
[50] C. Zhang, K.B. Hatzell, M. Boota, B. Dyatkin, M. Beidaghi, D. Long, W. Qiao, E. C. Kumbur, Y. Gogotsi, Highly porous carbon spheres for electrochemical capacitors and capacitive flowable suspension electrodes, Carbon 77 (2014) 155–164, https://doi.org/10.1016/j.carbon.2014.05.017.
[51] K.B. Hatzell, L. Fan, M. Beidaghi, M. Boota, E. Pomerantseva, E.C. Kumbur, Y. Gogotsi, Composite manganese oxide percolating networks as a suspension electrode for an asymmetric flow capacitor, ACS Appl. Mater. Interfaces 6 (2014) 8886–8893, https://doi.org/10.1021/am501650q.
[52] H. Hou, C.C. Sun, Quantifying effects of particulate properties on powder flow properties using a ring shear tester, J. Pharm. Sci. 97 (2008) 4030–4039, https://doi.org/10.1002/jps.21288.
[53] Q. Zhou, B. Armstrong, I. Larson, P.J. Stewart, D.A.V. Morton, Effect of host particle size on the modification of powder flow behaviours for lactose monohydrate following dry coating, dairy, Sci. Technol. 90 (2010) 237–251, https://doi.org/10.1051/dst/2009046.